

PAPER

A virtual-pinhole PET device for improving contrast recovery and enhancing lesion detectability of a one-meter-long PET scanner: a simulation study

To cite this article: Jianyong Jiang *et al* 2023 *Phys. Med. Biol.* **68** 145011

View the [article online](#) for updates and enhancements.


You may also like

- [Nanoscale mapping of shifts in dark plasmon modes in sub 10 nm aluminum nanoantennas](#)
Kenan Elibol, Clive Downing and Richard G Hobbs
- [A discussion on vacuum polarization, correction to the cross-section of \$e^+e^-\$](#)
Hong-Dou Jin, , Li-Peng Zhou et al.
- [Battery State of Health Model Estimation Based on Variable Projection Algorithm Using Steffensen Acceleration Method](#)
Lianyuan Cheng, Jing Chen, Yan Pu et al.



PAPER

A virtual-pinhole PET device for improving contrast recovery and enhancing lesion detectability of a one-meter-long PET scanner: a simulation study

RECEIVED
9 September 2022REVISED
5 May 2023ACCEPTED FOR PUBLICATION
19 June 2023PUBLISHED
10 July 2023Jianyong Jiang¹ , Jianlang Hua¹, Haihao Wang¹, Ziquan Yuan¹, Yuan Meng², Haoyu Lu², Steven Liu³, Yunlai Chen⁴ and Yuan-Chuan Tai^{5,*}¹ Key Laboratory of Beam Technology of Ministry of Education, College of Nuclear Science and Technology, Beijing Normal University, Beijing, People's Republic of China² School of Artificial Intelligence, Beijing Normal University, Beijing, People's Republic of China³ Renaissance School of Medicine, Stony Brook University, Stony Brook, New York, NY-11794, United States of America⁴ Imaging Science Program, Washington University in St. Louis, St. Louis, Missouri, MO-63110, United States of America⁵ Mallinckrodt Institute of Radiology, Washington University in St. Louis, St. Louis, Missouri, MO-63110, United States of America

* Author to whom any correspondence should be addressed.

E-mail: taiy@wustl.edu**Keywords:** long axial FOV PET scanner, virtual-pinhole PET, image reconstruction, lesion detection

Abstract

This paper presents a simulation study to demonstrate that the contrast recovery coefficients (CRC) and detectability of small lesions of a one-meter-long positron emission tomography (PET) scanner can be further enhanced by the integration of high resolution virtual-pinhole (VP) PET devices. The scanner under investigation is a Siemens Biograph Vision Quadra which has an axial field-of-view (FOV) of 106 cm. The VP-PET devices contain two high-resolution flat panel detectors, each composed of 2×8 detector modules each of which consists of 32×64 lutetium-oxyorthosilicate crystals ($1.0 \times 1.0 \times 10.0$ mm³ each). Two configurations for the VP-PET device placement were evaluated: (1) place the two flat-panel detectors at the center of the scanner's axial FOV below the patient bed; (2) place one flat-panel detector at the center of the first and the last quarter of the scanner's axial FOV below the patient bed. Sensitivity profiles were measured by moving a point ²²Na source stepwise across the scanner's FOV axially at different locations. To assess the improvement in CRC and lesion detectability by the VP-PET devices, an elliptical torso phantom ($31.6 \times 22.8 \times 106$ cm³) was first imaged by the native scanner then subsequently by the two VP-PET geometry configurations. Spherical lesions (4 mm in diameter) having 5:1 lesion-to-background radioactivity concentration ratio were grouped and placed at nine regions in the phantom to analyze the dependence of the improvement in plane. Average CRCs and their standard deviations of the 7 tumors in each group were computed and the receiver operating characteristic (ROC) curves were drawn to evaluate the improvement in lesion detectability by the VP-PET device over the native long axial PET scanner. The fraction of coincidence events between the inserts and the scanner detectors was 13%–16% (out of the total number of coincidences) for VP-PET configuration 1 and 2, respectively. The VP-PET systems provide higher CRCs for lesions in all regions in the torso, with more significant enhancement at regions closer to the inserts, than the native scanner does. For any given false positive fraction, the VP-PET systems offer higher true positive fraction compared to the native scanner. This work provides a potential solution to further enhance the image resolution of a long axial FOV PET scanner to maximize its lesion detectability afforded by its super high effective sensitivity.

1. Introduction

Positron emission tomography (PET) is a molecular imaging technique that has evolved from a highly exclusive research tool accessible in only selected medical centers to a widely available tool in many hospitals for the

detection of cancer metastasis and monitoring of treatment response (Gallagher *et al* 1977, Kuhl *et al* 1977, Gallagher *et al* 1978, Som *et al* 1980, Glaspy *et al* 1993, Nieweg *et al* 1993, Rege *et al* 1993, Knuuti and Nuutila 1999, Anand *et al* 2009, Weber 2010, Humbert *et al* 2015). Currently, PET/CT is commonly used in clinical oncology to visualize glucose metabolism in cancer. It has been long established that pretreatment imaging with PET/CT gives oncologists valuable insight into the prognosis of a cancer based on quantifiable metrics such as metabolic tumor volume (MTV), total lesion glycolysis (TLG), and standardized uptake value (SUV_{max}) for a wide range of cancer types (Im *et al* 2016, Chen *et al* 2017, Zhu *et al* 2017, Hwang *et al* 2017a, 2017b, Kim *et al* 2021). However, as a photon-deficient imaging technology, the utility of PET remains constrained by factors such as low signal-to-noise ratio, moderate spatial resolution, long scanning time and concerns about radiation dose (Budinger 1998, Slomka *et al* 2016, Berg and Cherry 2018, Zhang and Knopp 2020). Signal-to-noise ratio (SNR) of PET images is primarily driven by the number of 511 keV photon pairs detected while the spatial resolution of a commercial whole-body (WB) PET system is partly limited by the photon acollinearity effect, which accounts for the diameter of the PET system and the increased cost of the system associated with using smaller crystals (Moses and Derenzo 1993, Berg and Cherry 2018).

Extending the axial length of a typical clinical PET scanner offers the potential to dramatically enhance the sensitivity of PET (Cherry *et al* 2018, Badawi *et al* 2019, Pantel *et al* 2020, Tan *et al* 2020, Vandenberghe *et al* 2020, Zein *et al* 2020, Lan *et al* 2021), thereby improving the SNR of the PET images by: (1) covering a greater portion of the patients' body to collect more signals and (2) increasing the solid angle coverage of a particular organ in the patients' body. In a recent study (Cherry *et al* 2018), Cherry *et al* found that extending a WB PET scanner from a typical 20 cm axial field-of-view (FOV) to a 200 cm FOV (total body PET) increases the effective sensitivity by approximately 40 times (as measured by the noise-equivalent counting rate) for head-to-toe imaging and about 24 times for the more clinically common 'eyes to thighs' imaging. This gain presumably enhances not only the detectability of smaller or lower-contrast structures and lesions, but also improves the detection of lesion boundaries and allows for better quantification of volumes, thus allowing better estimates of MTV, TLG, and SUV_{max} in assessing disease prognosis. The sensitivity gain may be also used to reduce the typical 10–20 min imaging time of a clinical WB PET scan by a factor of 40—down to 15–30 s—while maintaining the same SNR. Finally, the long axial FOV scanner may be used for low dose imaging applications. This effective sensitivity gain can be further increased by improving the timing resolution of the detectors (Conti 2009, 2011, Surti 2015). Overall, recent studies have found that a long axial FOV scanner drastically improves both the sensitivity and temporal sampling capability of PET compared to previous-generation short axial FOV systems (Viswanath *et al* 2020, Alberts *et al* 2021, Spencer *et al* 2021). However, for a single bed position, the per-organ sensitivity gain is 2–3 times that of a conventional scanner and is limited to the center FOV of the scanner axially.

Even with ultra-high effective sensitivity in the center, a long axial FOV scanner still has its drawbacks. First, the spatial resolution of such a system has not been significantly improved. Assuming a ring diameter of >80 cm, the blurring from the so-called photon non-colinearity effect on the image resolution of a clinical WB-PET (including long axial FOV scanners) can be as much as ~ 2 mm full-width-at-half-maximum (FWHM) when accurate resolution models of point spread functions (PSF) were not applied to recover such physics effect. While the overall image resolution of a clinical WB-PET scanner can still be improved by using small crystals or detectors with depth of interaction technology, it is highly limited by the photon non-colinearity effect. By comparing the effects of detector intrinsic spatial resolution versus coincidence resolving time (CRT) on tumor detectability under WB imaging protocols, Surti *et al* (Kim *et al* 2021) found that both detectors of higher timing resolution and higher intrinsic spatial resolution improve lesion detectability. This work suggests that the imaging performance of PET is controlled and limited by system sensitivity under the WB imaging conditions. Furthermore, Jiang *et al* (Zhou and Qi 2009). Studied the effect of enhanced system sensitivity versus spatial resolution on tumor detectability of a biograph vision PET/CT scanner equipped with high-resolution outsert detectors and found that the enhancement of image performance from the outsert is due to both boosted system sensitivity and boosted image resolution, albeit predominantly the latter. Altogether, these findings prompted efforts to improve the spatial resolution of a long axial FOV PET scanner to further expand its potential applications in the study of human disease. Furthermore, the effective sensitivity of such a system at the edge in the axial direction is not improved as significantly compared to the center. Thus, the image quality is nonuniform in the axial direction. Therefore, technologies that selectively improve image resolution at the edge of a long axial FOV PET scanner may improve lesion detectability at the edge of the axial FOV thereby improving the overall performance of a total body PET scanner.

Zoom-in PET (Zhou and Qi 2009), multi-resolution PET (Clinthorne *et al* 2004, Park *et al* 2007a, 2007b), and virtual-pinhole PET (VP-PET) (Tai *et al* 2008) are technologies that improve the image resolution of a native PET scanner with a common approach in connecting a group of high-resolution detectors to the scanner and combining coincidences from the scanner itself and the region between the scanner and the insert. The photon detection efficiency is also increased when the high-resolution VP-PET detectors are placed close to the regions of interest. We previously reported the development of several VP-PET systems and their contribution to the

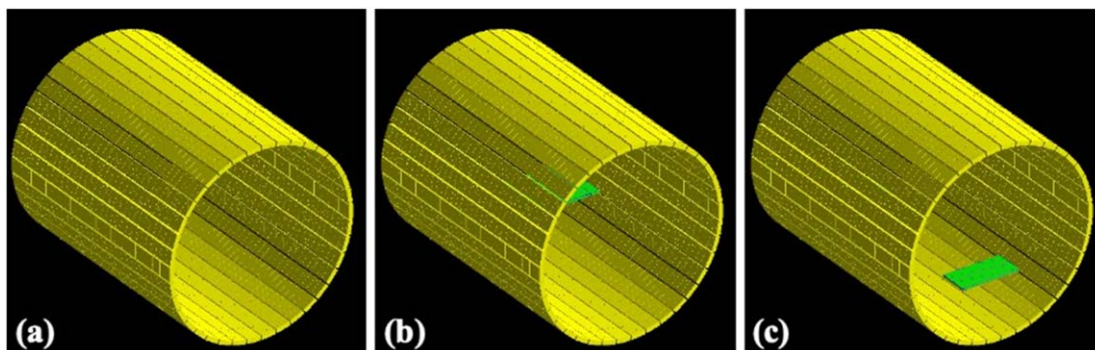


Figure 1. (a) A Siemens Biograph Vision Quadra with an axial field-of-view (FOV) of 106 cm; (b) A Siemens Biograph Vision Quadra equipped with one big panel insert; (c) a Siemens Biograph Vision Quadra equipped with two inserts placed at 1/8 and 7/8 of the scanner's axial FOV.

enhancement of lesion detectability of a PET scanner (Wu *et al* 2008, Mathews *et al* 2013, Jiang *et al* 2019a). In this work, we report the design of VP-PET devices to improve the uniformity of lesion detectability along the axial direction for a long axial FOV PET scanner. We used the Monte Carlo technique to simulate a torso phantom imaged by a Siemens Biograph Vision Quadra scanner equipped with different VP-PET devices. Images of the torso phantom were then produced using an image reconstruction software that runs on multiple graphics processing units (GPUs) based on the list mode maximum likelihood estimation maximization (MLEM) method (Li 2017, Jiang *et al* 2019a). Contrast recovery coefficient (CRC) and lesion detectability are analyzed to assess performance enhancement by the VP-PET devices.

2. Materials and methods

2.1. Monte carlo simulation

We used GATE (Jan *et al* 2004, Sarrut *et al* 2014, 2021) to evaluate the sensitivity and lesion detectability of a long axial FOV PET scanner both with and without VP-PET devices. In this study, the scanner used is a 106 cm axial FOV Siemens Biograph Vision Quadra (Prenosil *et al* 2022) which is composed of 1216 detector modules arranged in 32 rings with a radius of 422 mm. Each module consists of a lutetium-oxorthosilicate (LSO) array, each of which contains 20×10 crystals, with dimensions $3.2 \times 3.2 \times 20.0$ mm³. The native Quadra scanner uses 76 detector electronics assemblies (DEAs), of which each processes signals from 16 detector modules (8 rings \times 2/ring). We simulated two VP-PET systems as shown in figures 1(b) and (c) to evaluate the dependence of lesion detectability on the resolution of the one-meter-long scanner with ultra-high sensitivity. Both VP-PET systems contain two high-resolution flat-panel devices, each composed of 2×8 high-resolution detector modules, each of which is further composed of 32×64 $1.0 \times 1.0 \times 10.0$ mm³ sized LSO crystals. The total dimensions ($129 \times 263 \times 10$ mm³) of the LSO arrays in an insert are the same as one standard DEAs in the Biograph Vision Quadra scanner. In configuration 1, the two inserts are placed at (0, -195.0, -65.0) mm and (0, -195.0, 65.0) mm (configuring the center of the scanner's imaging FOV to (0, 0, 0) mm) to form a bigger flat-panel of length 130 mm at the axial center of the system. In configuration 2, the two inserts are placed at (0, -195.0, -396.0) mm and (0, -195.0, 396.0) mm to improve image resolution near the axial edges of the scanner's FOV. A torso phantom ($31.6 \times 22.8 \times 106$ cm³) was subsequently centered in the scanner's imaging FOV. Sixty-three spherical tumors (7 lesions in one group, as shown in figure 2(a)) were placed at the center of the scanner, as well as at the center of the edge quarter as shown in figures 2(b) and (c), respectively. The center of the edge quarter is 396 mm off from the scanner center axially. The diameter of the lesions was set to be 4 mm and 5 mm subsequently. The lesion-to-background ratio was 5 for the 4 mm lesion study and 3 for the 5 mm tumor study by filling ¹⁸F solutions in the torso phantom and lesion with an initial activity concentration of 5.3 kBq ml⁻¹ in the background. Both scanner and insert detectors were assumed conservatively to have a CRT of 250 ps (FWHM) and energy resolution of 12% at 511 keV (FWHM). The energy window in the simulation was 435–650 keV. Scatter and random events were excluded to produce images. All cross-coincidences were accepted in the image reconstruction.

2.2. Imaging reconstruction

A general-purpose reconstruction framework that can reconstruct images under arbitrary spatial placements of detector crystals with different dimensions to support the asymmetric and unconventional geometry of VP-PET

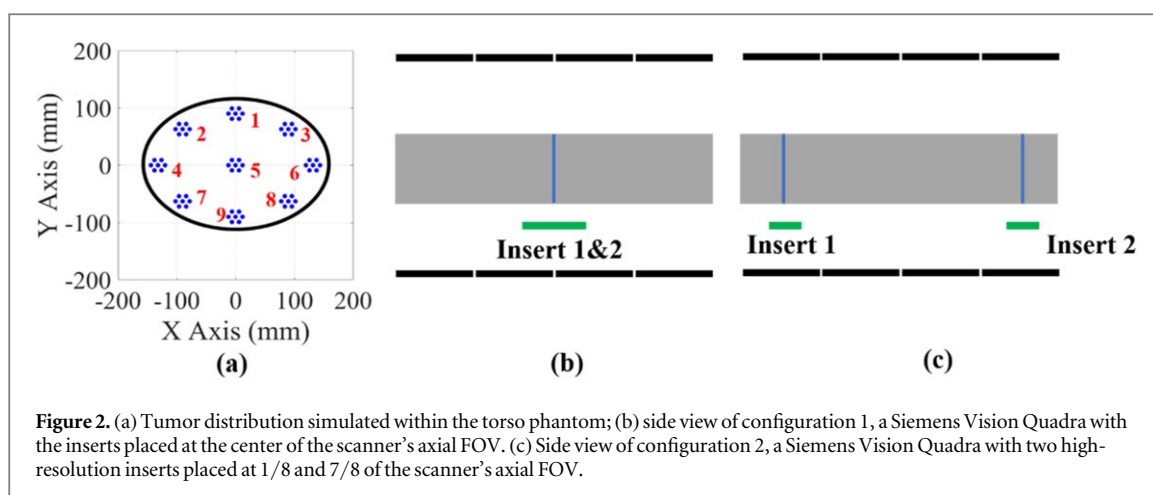


Table 1. Enhancement in sensitivity by the VP-PET devices.

Configurations	Configuration 1			Configuration 2		
	IS/Total	SS/Total	Total/ScannerOnly	IS/Total	SS/Total	Total/ScannerOnly
Y = -100 mm	14.24%	85.76%	103.27%	11.55%	88.45%	106.58%
Y = 0 mm	7.93%	92.07%	101.40%	6.63%	93.37%	103.43%
Y = 100 mm	5.91%	94.09%	101.24%	4.94%	95.06%	102.51%

devices has been developed (Mathews *et al* 2015). An image reconstruction software based on list mode MLEM algorithm running on multiple GPUs (Huh *et al* 2009, Cui *et al* 2011, Praxt *et al* 2011a, 2011b) to compute the system matrix on-the-fly already exists (Jiang *et al* 2019b). The quantitative accuracy of this framework was evaluated in an imaging study that uses a Siemens Biograph Vision PET/CT scanner to scan a National Electrical Manufacturers Association (NEMA) image quality (IQ) phantom and compares its images reconstructed using this framework versus Siemens's software (e7 tools) using the OP-OSEM-TOF method (Samanta *et al* 2021). Forward projection of the attenuation coefficient map of the known geometry of the object was used to correct for attenuation, which in practice can be obtained via CT images (Keesing *et al* 2012). The attenuation of the inserts was also included in the attenuation correction. The overall geometric effect and the individual crystal efficiency were considered in the component-based normalization (Keesing *et al* 2012, Samanta *et al* 2021). Images are reconstructed using prompt events in a 3D rectilinear space of $400 \times 400 \times 1060$ cubic voxels, with each voxel $1 \times 1 \times 1 \text{ mm}^3$. TOF information was used to reconstruct simulated data; random and scatter corrections were not applied in the reconstruction of the 3D images.

2.3. Sensitivity profile

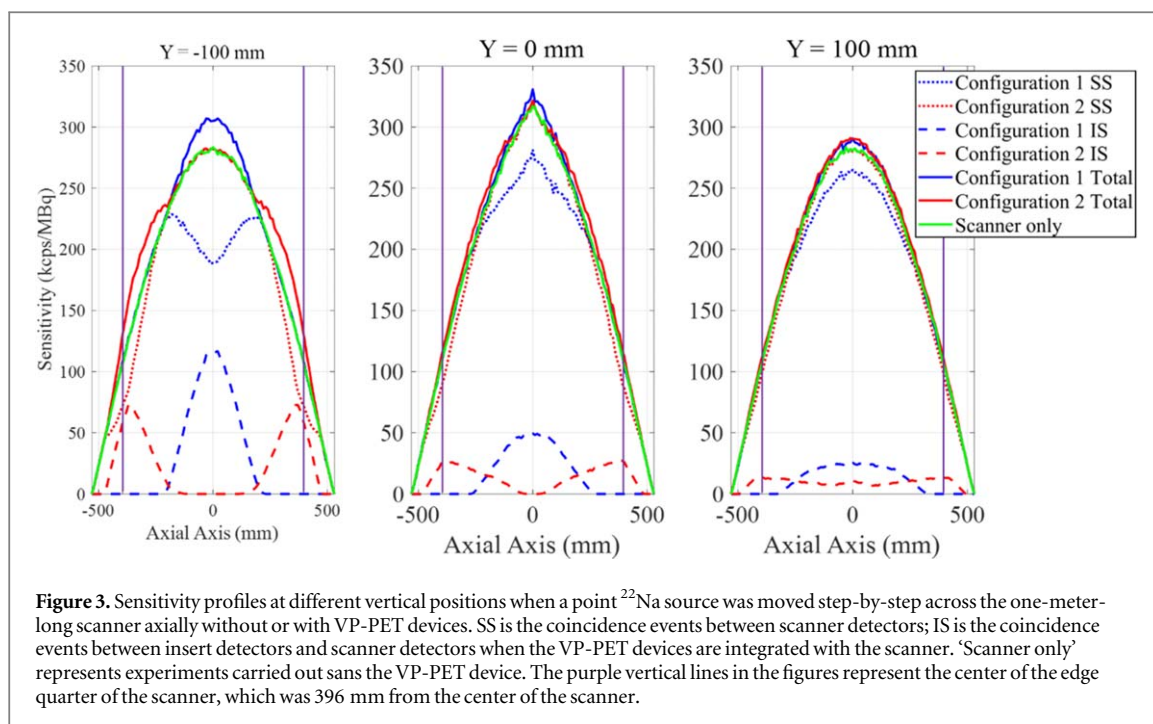
To measure the sensitivity profile of the simulated systems, a point ^{22}Na source was moved stepwise across the axial FOV of the scanner at different vertical locations ($Y = -100, 0, \text{ or } 100 \text{ mm}$). To characterize the sensitivity of the scanner without or with the VP-PET devices, the portion of coincidence events acquired by different detector groups was measured (Scanner-Scanner—SS, Scanner-Insert—IS) as specified in table 1. The total number of prompt coincidence events acquired by the scanner and the inserts were normalized to the number of decays from the ^{22}Na source. We plotted the sensitivity profiles as a function of the source location across the axial FOV.

2.4. Contrast recovery coefficient and receiver operating characteristic

The CRC for every known lesion was computed to quantify the performance of the scanner without or with the VP-PET devices when used for small lesion and structure detection. Using the NEMA NU2–2018 standard (Association 2018), CRC_i for the i th spherical tumor was computed:

$$\text{CRC}_i = 100\% \times \frac{\left(\frac{C_{t,i}}{C_b} - 1 \right)}{(\text{uptake} - 1)}. \quad (1)$$

Here, $C_{t,i}$ is the mean count density in the i th lesion and was estimated by drawing a spherical ROI over the center of the corresponding sphere in the image volume. The diameter of the ROI is 4 mm, which is the same as



the diameter of the spherical lesion under evaluation. Within an ROI, the average count was computed by summing the weighted counts in voxels overlapping with the ROI. Count density of the background, C_b , was calculated using the average counts of voxels in a 3D cubic ROI drawn from 20 adjacent slices. Uptake is the tumor-to-background ratio which is 5 in this study. The average CRCs and standard deviation of the seven lesions in each group are reported in this simulation study.

To further compare the lesion detectability of the scanner with versus without the VP-PET devices, ROC curves (Hajian-Tilaki 2013) were constructed by plotting the true positive fraction (TPF) as a function of the false positive fraction (FPF). For a given threshold, TPF was determined by the number of lesions with mean count densities higher than the threshold divided by the total number of lesions. The FPF was determined by the number of all possible ROIs having the same dimension as the lesions under evaluation with mean count densities higher than the threshold divided by the total number of all possible spherical ROIs in the image volume. A hexagonal grid was selected and drawn over the entire 3D image volume and spherical ROIs with dimensions of the lesions were drawn at all vertexes within the phantom of the hexagonal grid to calculate the mean count density, allowing us to calculate TPF and FPF against all possible threshold values (Linnet 1987, Hanley 1989).

3. Results

3.1. Sensitivity profile

Figure 3 shows the sensitivity profile of the scanner with or without VP-PET devices when a point ^{22}Na source was moved step-by-step across the FOV axially at different vertical positions ($Y = 100$ mm, $Y = 0$ mm, and -100 mm). By computing the area under the curves (AUC) of sensitivity profiles in comparison, the overall sensitivity improvement for configurations 1 and 2 over the native Quadra scanner was evaluated. Results are presented in table 1. The fractions of IS events are 14.24%, 7.93%, and 5.91% when $Y = -100$, $Y = 0$, and $Y = 100$ mm, respectively in configuration 1. The overall sensitivity enhancements of configuration 1 over the native scanner were 3.27%, 1.40%, and 1.24% when $Y = -100$, $Y = 0$, and $Y = 100$ mm. The fractions of IS events are 11.55%, 6.63%, and 4.94% when $Y = -100$, $Y = 0$, and $Y = 100$ mm, respectively in configuration 2. The overall enhancements of configuration 2 over the native scanner were 6.58%, 3.43%, and 2.51% when $Y = -100$, $Y = 0$, and $Y = 100$ mm.

3.2. Lesion detectability

Coincidence events were acquired using the Quadra scanner for 180 s first then using the other two VP-PET systems as shown in figures 1(b) and (c) subsequently. Images were produced using the MLEM-based image reconstruction code with different simulated scan durations of 30–180 s for the three simulated systems.

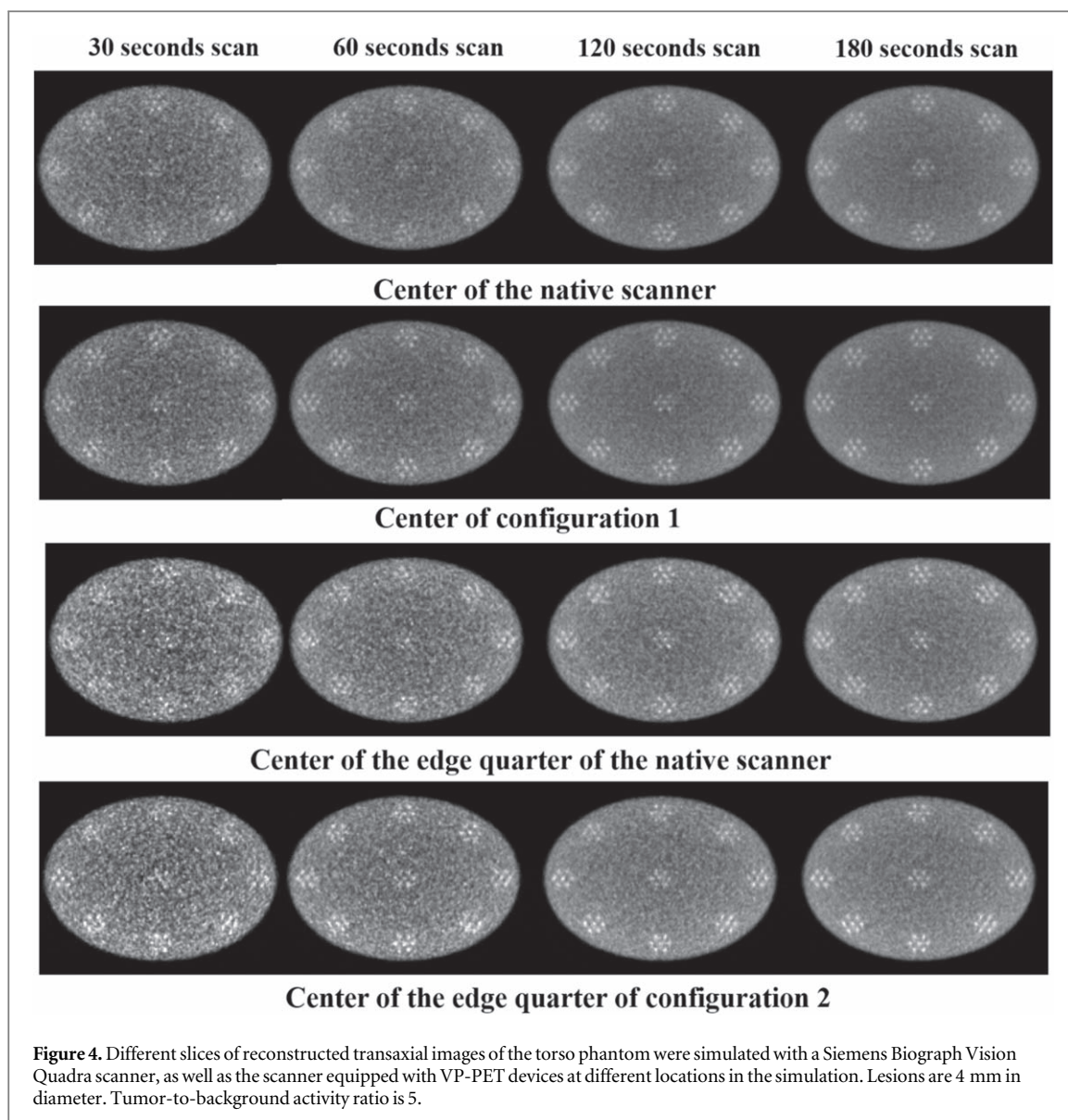


Figure 4 illustrates the reconstructed transaxial images of the torso phantom scanned with different system configurations and scan times when the lesions were 4 mm in diameter. From left to right, columns represent scan times of 30 s, 60 s, 120 s, and 180 s after 30 iterations. From top to bottom, rows represent images captured at the center by the native scanner, at the center by configuration 1, at the center of the edge quarter (one-eighth the axial FOV from an edge) by the native scanner, and at the center of the edge quarter by configuration 2.

Mean CRCs of the 7 lesions in each group of all the reconstructed images were computed to further quantify the enhancement by the VP-PET devices. The results are shown in figure 5. Figure 5(a) shows the comparison of the average CRCs of the 7 tumors in each group at the center and at the edge. Tumors gain higher contrast recovery in the center than at the edge when the scan time is 30 s. However, tumors at the edge gain higher contrast recovery with 120 s and 180 s scans. This suggests that the axial resolution at the edge is higher compared to the center of the long scanner due to lower parallax error. The average CRCs are 0.12 ± 0.05 , 0.11 ± 0.02 , and 0.11 ± 0.02 for tumors in region 5 in center slices and 0.09 ± 0.06 , 0.15 ± 0.04 , and 0.16 ± 0.04 for tumors in the same region at the center of the edge quarter in the native scanner under 30 s, 120 s, and 180 s scan, respectively. CRCs of the tumors at the center of the native scanner were improved by the large panel detector in configuration 1 while CRCs of the tumors at the center of the edge quarter were also enhanced by the insert detectors in configuration 2. The enhancement was more significant for the tumors that are closer to the panel. For example, for a 120 s scan, the CRCs of the tumors in regions 7, 8, and 9 were 0.06 ± 0.01 , 0.09 ± 0.01 , and 0.10 ± 0.01 in the center slice of the native scanner image. These values were improved to 0.12 ± 0.02 , 0.17 ± 0.02 , and 0.16 ± 0.02 respectively when using the VP-PET insert in configuration 1.

Comparing the first row (center slice without VP-PET) versus the second row (center slice with VP-PET) of the images in figure 4 demonstrates a contrast improvement with the addition of the VP-PET device from

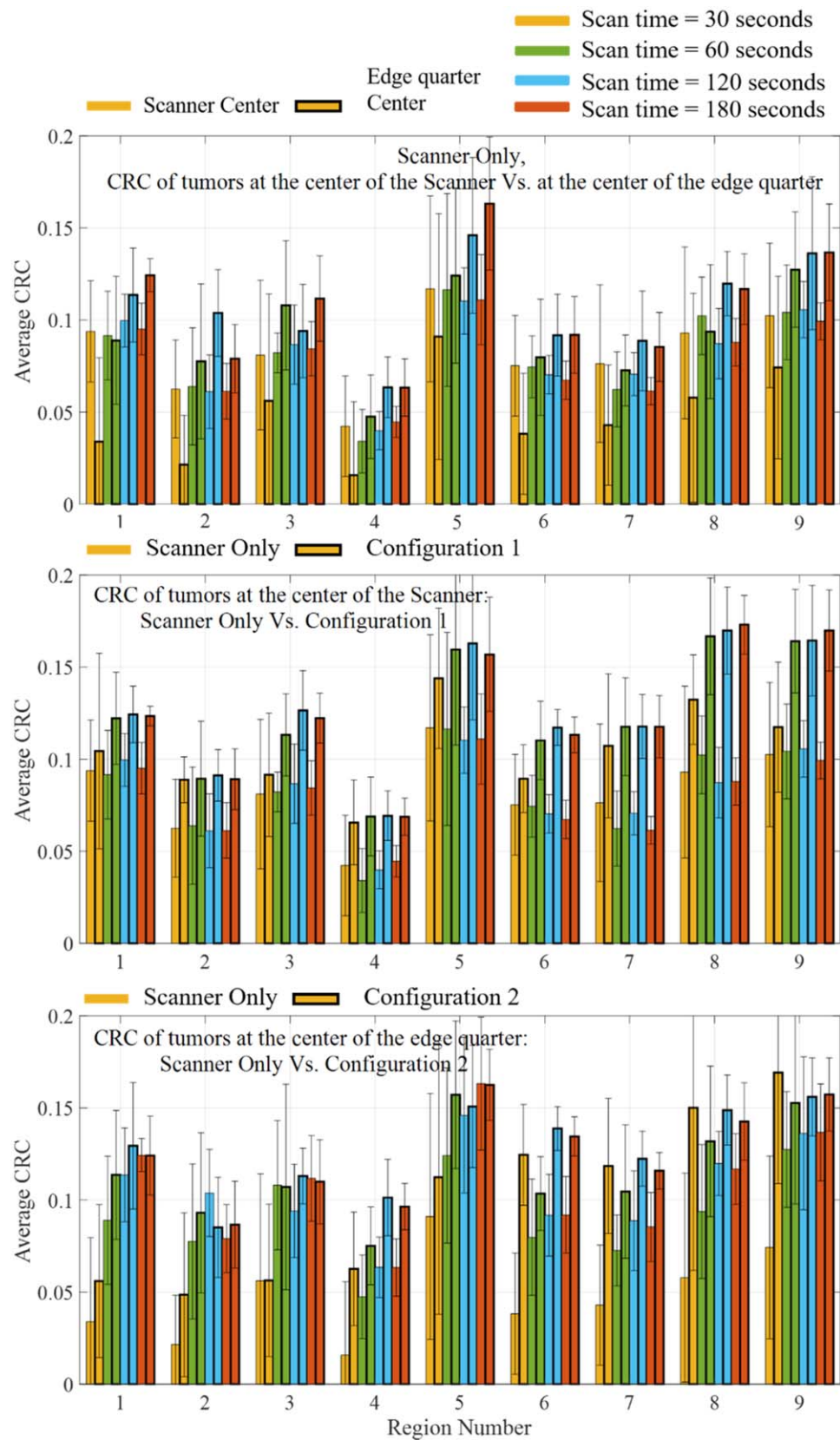


Figure 5. Comparison of average CRCs of 7 tumors in different regions of images from (a) scanner center and edge quarter center of the native scanner; (b) center slice of the native scanner and configuration 1; (c) edge quarter center of the native scanner and configuration 2.

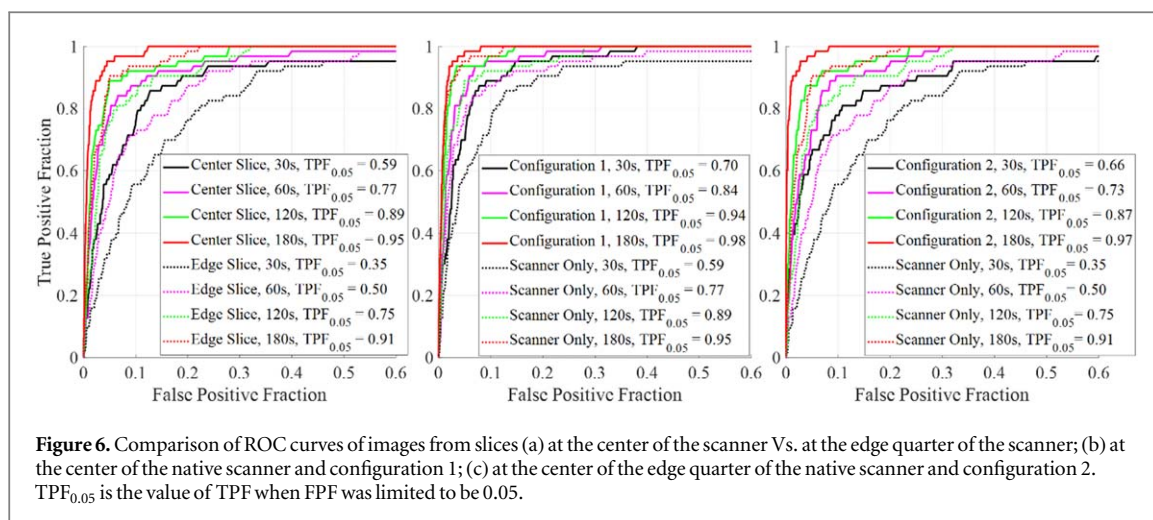


figure 1(b). Similarly, comparing the third row versus the fourth row demonstrates a contrast improvement with the addition of the VP-PET device from figure 1(c). Altogether, the addition of VP-PET technology to a long axial FOV PET scanner allows for a visible contrast improvement compared to the native scanner alone.

Figure 6(a) shows the comparison of ROC curves of images at the center and at the center of the edge quarter of the native scanner under different imaging times. As expected, longer scanning times corresponded to the higher tumor detectability. The scanner provides higher tumor detectability in the center compared to the edge axially.

Figure 6(b) shows the comparison of ROC curves of images in the first and second rows in figure 4 across different scan times. With a flat-panel VP-PET device in the center of the long axial scanner, tumors in the center slice were resolved more clearly compared to by the native scanner alone. As shown in figure 6(b), for any given FPF, configuration 1 offers higher TPF compared to the native PET scanner. For instance, $TPF_{0.05}$ (value of TPF when $FPF = 0.05$) for the native scanner at the center slice for 30 s, 60 s, 120 s, and 180 s imaging times is 0.59, 0.77, 0.89 and 0.95, respectively. The $TPF_{0.05}$ is improved to 0.70, 0.84, 0.94 and 0.98 by the flat-panel inserts in configuration 1.

Figure 5(c) shows the comparison of ROC curves of images in the third and fourth rows in figure 4 under different scan times. As shown in figure 5(c), for any given FPF, configuration 2 also offers a higher TPF compared to the native Quadra PET scanner in the edge slice. For instance, the $TPF_{0.05}$ is 0.35, 0.50, 0.75, 0.91 for the native scanner for 30 s, 60 s, 120 s, and 180 s scans respectively. The $TPF_{0.05}$ is improved to 0.66, 0.73, 0.87, and 0.97 by the flat-panel devices in configuration 2.

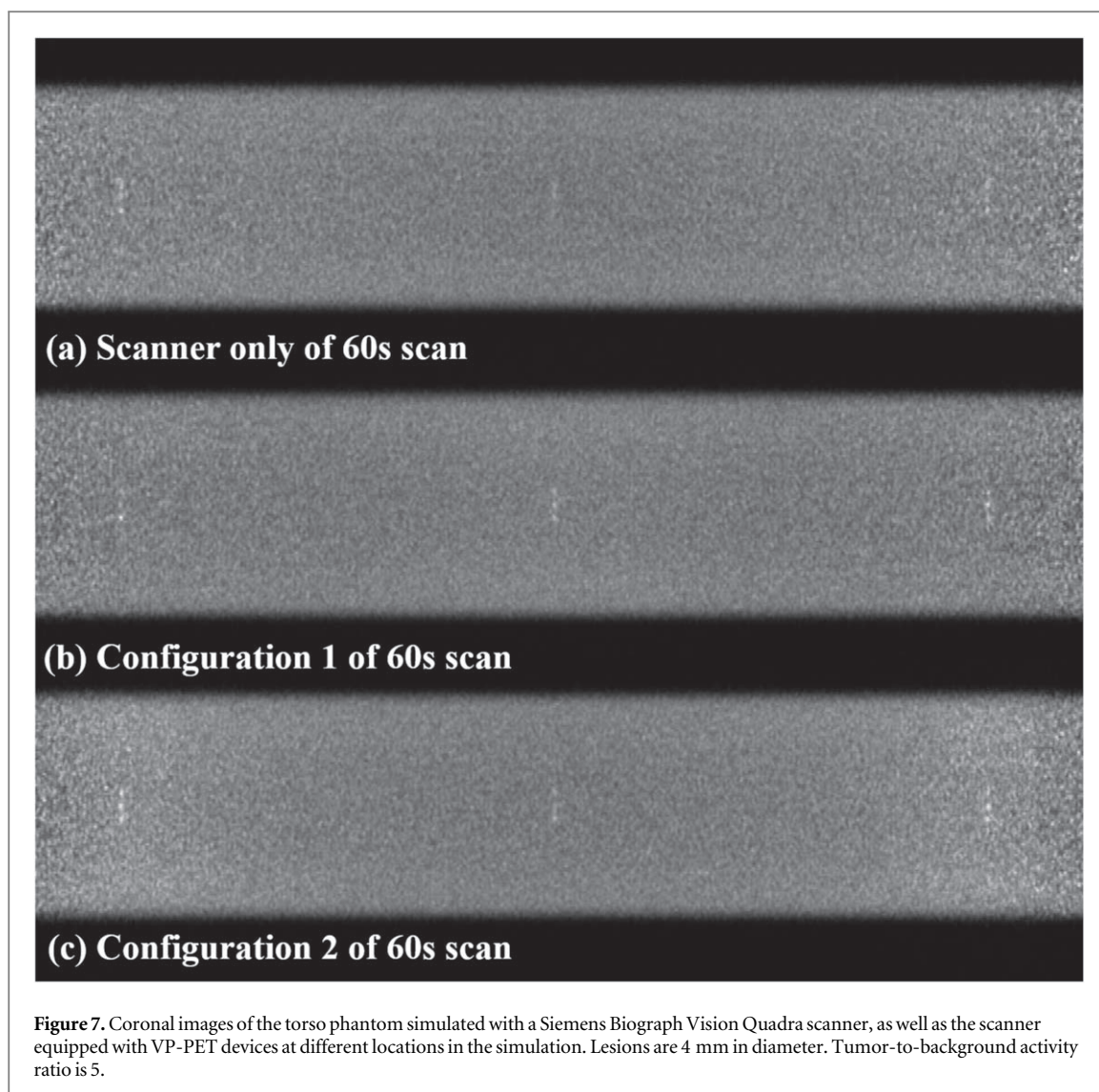
Figure 7 illustrates the reconstructed coronal images of the torso phantom by different system configurations of the 60 s scan. Tumors shown in the images are the three lesions in the second row of group 9 in 3 different slices. From top to bottom, images were captured by the native scanner, in configuration 1 and 2, respectively. For the image under 60 s scan by the native scan, the tumors at the edge were observed more clearly axially than those in the center. This implies that the axial image resolution in the center of a long scanner was degraded by the parallax error compared to that at the edge. As illustrated in figures 7(b) and (c), visual enhancement of the contrast recovery was observed for tumors at the center of the native scanner by the large panel detector in configuration 1 and for tumors at the center of the edge quarter by the insert detectors in configuration 2.

The reconstructed transaxial images of 60 s scan and 180 s scans when the lesion diameter was 5 mm were shown in figure 8(a). From left to right, columns represent scan times of 60 s and 180 s after 30 iterations. From top to bottom, rows represent images captured at the center by the native scanner, at the center by configuration 1, at the center of the edge quarter by the native scanner, and at the center of the edge quarter by configuration 2.

Comparisons of ROC curves were shown in figures 8(b) and (c). As shown in the images in figure 8(a), visual improvement of contrast recovery of the lesions at the center and that of lesions at the edge was observed in configuration 1 and configuration 2, respectively. ROC curves in figures 8(b) and (c) demonstrate similar results as illustrated in figure 5 that the tumor detectability of lesions of 5 mm in diameter can be improved by improving the image resolution via VP-PET technology.

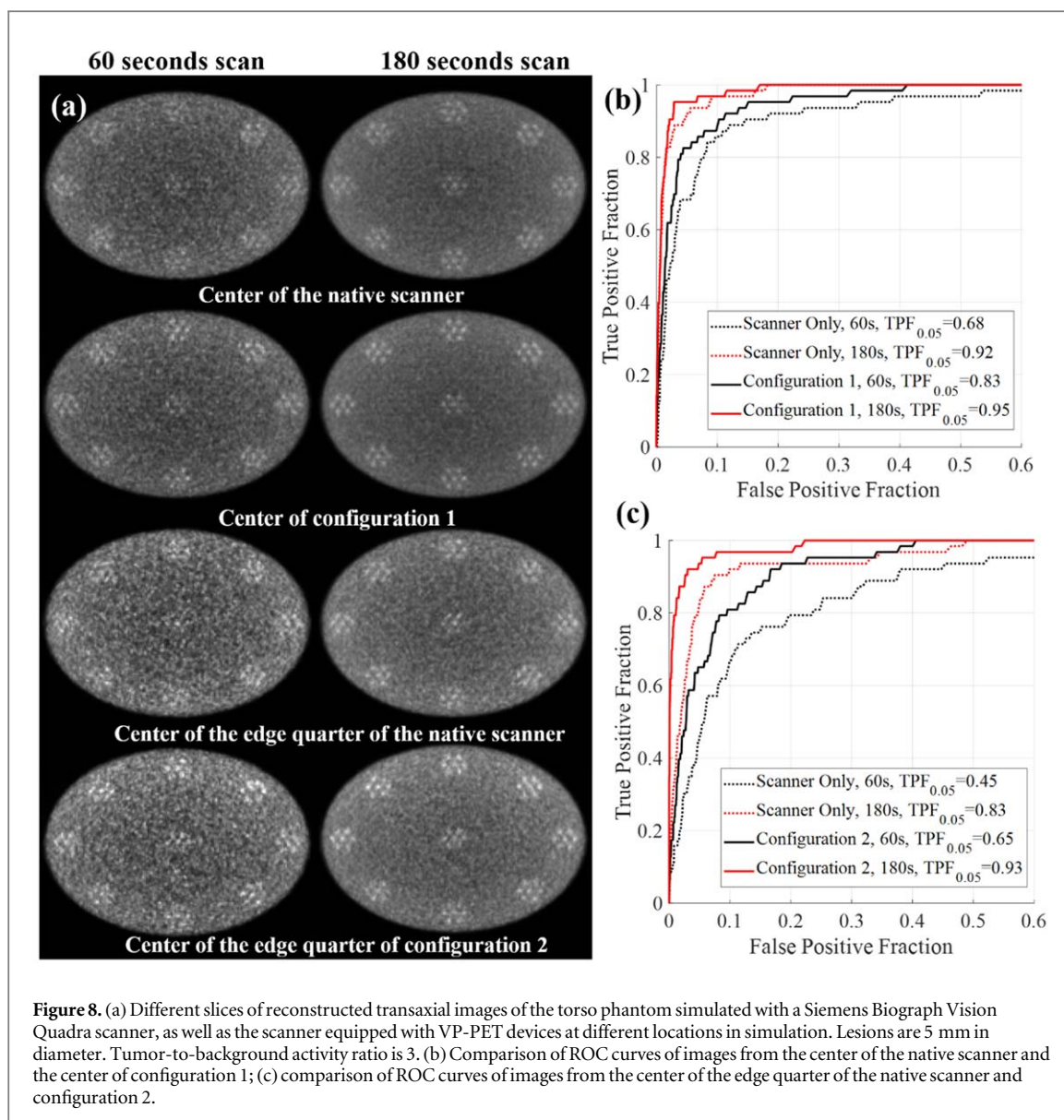
4. Discussion

With Ultra-high sensitivity, a long axial FOV PET scanner may enable new applications of PET both in clinical research and in patient care. However, given a ring diameter larger than 80 cm and without applying an accurate



resolution/PSF model, the spatial resolution of WB-PET is limited to be no better than ~ 2 mm (FWHM) by the photon acolinearity effect. The 511 keV gamma rays traveling along the axial direction may enter a detector array at a large oblique angle resulting in significant crystal penetration and parallax error that can compromise the image resolution of a long axial FOV PET scanner. In this work, we proposed flat-panel insert devices for enhancing contrast recovery and improving lesion detectability via VP-PET technology. CRCs of spherical lesions at different regions and ROC curves of different systems were analyzed in comparison to reflect the validity of the VP-PET technology. Without a close-form analytical reconstruction method to model the asymmetric geometries of VP-PET systems in this study, the image resolution of a VP-PET system and that of a native PET scanner can be quantitatively compared with each other by subtracting a uniform background from the statistically calculated images.

We observed remarkable enhancement in contrast recovery and tumor detectability of small structures in selected target regions by the flat-panel VP-PET insert devices. Further improvements to the overall system image resolution and/or sensitivity involve optimizing the design of the insert detectors, which is often a trade-off between the desired performance and cost-effectiveness and is constrained by other design considerations such as mechanical integration to the native scanner and image correction techniques. The choice of detector technology will first need to match the insert detector performance to that of the scanner detectors to avoid system re-development. For example, as we are trying to achieve high intrinsic detector spatial resolution, the timing resolution of the insert detector needs to have a comparable performance with that of the scanner detector to take advantage of the TOF-PET features. The decision of crystal dimensions of the insert detectors is also the result of the consideration of the detection sensitivity versus system resolution. A shorter crystal length will mitigate the parallax effect at the cost of sensitivity degradation of IS event detection. If the total number of readout electronics is limited by the design of the firmware or hardware, a larger crystal-section will increase the solid angle coverage of the VP-PET detector thus enhancing the overall system sensitivity at the expense of



resolution degradation. As a result, various factors will need to be taken into consideration cautiously for designing the actual insert detectors optimally before the implementation of a VP-PET system. For future commercial devices, further studies to determine the most cost-effective design for the proposed VP-PET technology need to be conducted.

Based on the location of tumors, or the target locations for the scan, the detector arrangement could be further optimized. For instance, given a primary tumor diagnosis of breast cancer, there is a relatively high chance of metastatic spread to the ovaries and liver compared to other sites. Thus, we can take advantage of known metastatic patterns of different cancers, which has been long established in literature, to selectively enhance the resolution of sites at which there is a higher chance of cancer spread in an effort to reduce the number of occult metastases that go undetected (Budczies *et al* 2015). Moreover, VP-PET may yield specific benefits for certain types of cancer; in non-small-cell lung cancer (NSCLC), for example, an increased resolution at the pulmonary lesions may help to more accurately stage NSCLC and reduce the number of stage-inappropriate surgeries (Fischer *et al* 2009, Maziak *et al* 2009).

One challenge related to the targeted placement of insert detectors may be the size of a patient's body that could hinder us from placing detectors at desired locations given the limited space in the patient port. Therefore, the image quality of VP-PET insert systems should be further studied to optimize the imaging protocol given such a space constraint in the placement of the insert.

A long axial FOV scanner drastically improves the sensitivity gain, especially at the center of the scanner. However, the axial image resolution is degraded at the center compared to that at the edge, due to the parallax error. Because of the degradation, the CRCs of lesions at the center are lower than those at the edge. The tumor detectability is higher at the center of the scanner compared to the edge of the scanner axially. A high-resolution

Table 2. TPF_{0.05} of ROC curves in figure 5.

Period	30 s	60 s	120 s	180 s
Center slice of native scanner	0.59	0.77	0.89	0.95
Center slice of configuration 1	0.70	0.84	0.94	0.98
Center of the edge quarter of native scanner	0.35	0.50	0.75	0.91
Center of the edge quarter of configuration 2	0.66	0.73	0.87	0.97

insert placed at the center of the scanner, e.g. in configuration 1, enhanced the image resolution of regions in the center of the scanner, thus enhancing the CRCs and lesion detectability of the lesions located in this region.

Table 2 listed the TPF_{0.05} of ROC curves in figure 5. As we can notice, the values of TPF_{0.05} at the center of the edge quarter of configuration 2 was comparable with those at the center of the native scanner. This suggests that the uniformity of lesion detectability along the axial direction was improved by placing high-resolution VP-PET devices at the center of the edge quarter.

All images were produced using a GPU-based list-mode MLEM framework where component-based normalization has been implemented. The normalization in the software was simplified and only took geometric effects and individual crystal efficiency into account. To reconstruct fully quantitative images from the VP-PET systems, other components such as dead time parameter, the crystal interference pattern of the insert detectors, and axial effects ought to be included in the future. With a device of approximately 10 mm thick close to the imaging target, scatter and random corrections must also be applied for the GPU-based image reconstruction framework.

5. Conclusion

In this work, we carried out a simulation study to compare the performance in terms of lesion contrast recovery and detectability of a one-meter-long PET scanner with and without VP-PET devices. Results show that even with ultra-high sensitivity of a PET scanner with extended axial length, the image performance can be further improved by improving the image resolution via VP-PET technology. The image qualities can be further enhanced by optimizing the design and arrangements of the insert detectors. This work provides a potential solution to further enhance the image resolution of a long axial FOV PET scanner to maximize its lesion detectability afforded by its super high effective sensitivity.

Images reconstructed using the current list mode GPU-based framework are semi-quantitative without appropriate correction techniques, e.g. normalization, scatter correction as well as random correction, which will be implemented in the future.

Acknowledgments

This work was supported in part by the National Natural Science Foundation of China (No. 12105018), Beijing Nova Program (No. Z211100002121129), and Beijing Normal University Start-up Grant (No. 312232104).

Data availability statement

The data cannot be made publicly available upon publication because no suitable repository exists for hosting data in this field of study. The data that support the findings of this study are available upon reasonable request from the authors.

Disclosure

The authors have no relevant conflicts of interest to disclose.

ORCID iDs

Jianyong Jiang  <https://orcid.org/0000-0001-6482-5915>

References

- Alberts I *et al* 2021 Clinical performance of long axial field of view PET/CT: a head-to-head intra-individual comparison of the biograph vision quadra with the biograph vision PET/CT *Eur. J. Nucl. Med. Mol. Imaging* **48** 2395–404
- Anand S, Singh H and Dash A 2009 Clinical applications of PET and PET-CT *Med. J. Armed Forces India* **65** 353–8
- Association N E M 2018 NEMA standards publication NU 2–2018: performance measurements of positron emission tomographs Rosslyn, Virginia, USA.
- Badawi R D *et al* 2019 First human imaging studies with the EXPLORER total-body PET scanner *J. Nucl. Med.* **60** 299–303
- Berg E and Cherry S R 2018 Innovations in instrumentation for positron emission tomography *Semin. Nucl. Med.* **48** 311–31 WB Saunders
- Budczies J *et al* 2015 The landscape of metastatic progression patterns across major human cancers *Oncotarget* **6** 570–83
- Budinger T F 1998 PET instrumentation: what are the limits? *Semin. Nucl. Med.* **28** 247–67 WB Saunders
- Chen L, Wu X, Ma X, Guo L, Zhu C and Li Q 2017 Prognostic value of 18F-FDG PET-CT-based functional parameters in patients with soft tissue sarcoma: a meta-analysis *Medicine (Baltimore)* **96** e5913
- Cherry S R, Jones T, Karp J S, Qi J, Moses W W and Badawi R D 2018 Total-body PET: maximizing sensitivity to create new opportunities for clinical research and patient care *J. Nucl. Med.* **59** 3–12
- Clinthorne N H, Sangjune P, Rogers W L and Ping-Chun C 2004 Multi-resolution image reconstruction for a high-resolution small animal PET device 2003 *IEEE Nuclear Science Symp.. Conf. Record (IEEE Cat. No.03CH37515)* pp 1997–2001 Vol 3 |lii+3759
- Conti M 2009 State of the art and challenges of time-of-flight PET *Phys. Med.* **25** 1–11
- Conti M 2011 Focus on time-of-flight PET: the benefits of improved time resolution *Eur. J. Nucl. Med. Mol. Imaging* **38** 1147–57
- Cui J Y, Prax G, Prevrhal S and Levin C S 2011 Fully 3D list-mode time-of-flight PET image reconstruction on GPUs using CUDA *Med. Phys.* **38** 6775–86
- Fischer B *et al* 2009 Preoperative staging of lung cancer with combined PET-CT *N. Engl. J. Med.* **361** 32–9
- Gallagher B M *et al* 1977 Radiopharmaceuticals XXVII. 18F-labeled 2-deoxy-2-fluoro-d-glucose as a radiopharmaceutical for measuring regional myocardial glucose metabolism *in vivo*: tissue distribution and imaging studies in animals *J. Nucl. Med.* **18** 990–6
- Gallagher B M, Fowler J S, Guttererson N I, MacGregor R R, Wan C N and Wolf A P 1978 Metabolic trapping as a principle of radiopharmaceutical design: some factors responsible for the biodistribution of [18F] 2-deoxy-2-fluoro-D-glucose *J. Nucl. Med.* **19** 1154–61
- Gaspy J A, Hawkins R, Hoh C K and Phelps M E 1993 Use of positron emission tomography in oncology *Oncology* **7** 41–55
- Hajian-Tilaki K 2013 Receiver operating characteristic (ROC) curve analysis for medical diagnostic test evaluation *Caspian J. Intern. Med.* **4** 627
- Hanley J A 1989 Receiver operating characteristic (ROC) methodology: the state of the art. *Crit. Rev. Diagn Imaging* **29** 307–35
- Huh S S, Han L, Rogers W L and Clinthorne N H 2009 Real time image reconstruction using GPUs for a surgical PET imaging probe system 2009 *IEEE Nuclear Science Symp. Conf. Record (NSS/MIC)* pp 4148–53
- Humbert O *et al* 2015 Role of positron emission tomography for the monitoring of response to therapy in breast cancer *Oncologist* **20** 94–104
- Hwang S H, Cho A, Yun M, Choi Y D, Rha S Y and Kang W J 2017a Prognostic value of pretreatment metabolic tumor volume and total lesion glycolysis using 18F-FDG PET/CT in patients with metastatic renal cell carcinoma treated with anti-vascular endothelial growth factor-targeted agents *Clin. Nucl. Med.* **42** e235–41
- Hwang S H, Lee J W, Cho H J, Kim K S, Choi G H and Yun M 2017b Prognostic value of metabolic tumor volume and total lesion glycolysis on preoperative 18F-FDG PET/CT in patients with very early and early hepatocellular carcinoma *Clin. Nucl. Med.* **42** 34–9
- Im H J *et al* 2016 Prognostic value of metabolic and volumetric parameters of preoperative FDG-PET/CT in patients with resectable pancreatic cancer *Medicine (Baltimore)* **95** e3686
- Jan S *et al* 2004 GATE: a simulation toolkit for PET and SPECT, *Phys. Med. Biol.* **49** 4543
- Jiang J *et al* 2019a A second-generation virtual-pinhole PET device for enhancing contrast recovery and improving lesion detectability of a whole-body PET/CT scanner *Med. Phys.* **46** 4165–76
- Jiang J, Li K, Komarov S, O'Sullivan J A and Tai Y C 2019a Feasibility study of a point-of-Care PET system with interactive imaging capability *Med. Phys.* **46** 1798–813
- Jiang J, Li K, Komarov S, O'Sullivan J A and Tai Y C 2019b Feasibility study of a point-of-care positron emission tomography system with interactive imaging capability *Med. Phys.* **46** 1798–813
- Keesing D B *et al* 2012 Image reconstruction and system modeling techniques for virtual-pinhole PET insert systems *Phys. Med. Biol.* **57** 2517–38
- Kim Y L, Lee H S and Choi J Y 2021 Prognostic significance of pretreatment 18F-FDG PET/CT volumetric parameters in patients with colorectal liver metastasis: a systematic review and meta-analysis *Clin. Nucl. Med.* **46** 206–13
- Knuuti J and Nuutila P 1999 PET as a cardiovascular and metabolic research tool *Ann. Med.* **31** 450–6
- Kuhl D E, Phelps M E, Hoffman E J, Robinson G D Jr and MacDonald N S 1977 Initial clinical experience with 18F-2-fluoro-2-deoxy-d-glucose for determination of local cerebral glucose utilization by emission computed tomography *Acta Neurol. Scand. Suppl.* **64** 192–3
- Lan X, Younis M H, Li K and Cai W 2021 First clinical experience of 106 cm, long axial field-of-view (LAFOV) PET/CT: an elegant balance between standard axial (23 cm) and total-body (194 cm) systems *Eur. J. Nucl. Med. Mol. Imaging* **48** 3755–9
- Li K 2017 Novel PET systems and image reconstruction with actively controlled geometry Washington University in St. Louis PhD Thesis
- Linnet K 1987 Comparison of quantitative diagnostic tests: type I error, power, and sample size *Stat. Med.* **6** 147–58
- Mathews A J *et al* 2015 A generalized reconstruction framework for unconventional PET systems *Med. Phys.* **42** 4591–609
- Mathews A J, Komarov S, Wu H, O'Sullivan J A and Tai Y C 2013 Improving PET imaging for breast cancer using virtual pinhole PET half-ring insert *Phys. Med. Biol.* **58** 6407–27
- Maziak D E *et al* 2009 Positron emission tomography in staging early lung cancer: a randomized trial *Ann. Intern. Med.* **151** 221–8
- Moses W W and Derenzo S E 1993 Empirical observation of resolution degradation in positron emission tomographs utilizing block detectors *J. Nucl. Med.* **34** 101P–01P 01/01
- Nieweg O E *et al* 1993 Positron emission tomography with fluorine-18-deoxyglucose in the detection and staging of breast cancer *Cancer* **71** 3920–5
- Pantel A R *et al* 2020 PennPET Explorer: human imaging on a whole-body imager *J. Nucl. Med.* **61** 144–51
- Park S J *et al* 2007b Performance evaluation of a very high resolution small animal PET imager using silicon scatter detectors *Phys. Med. Biol.* **52** 2807–26
- Park S J, Rogers W L and Clinthorne N H 2007a Design of a very high-resolution small animal PET scanner using a silicon scatter detector insert *Phys. Med. Biol.* **52** 4653–77

- Pratx G, Cui J-Y, Prevrhal S and Levin C S 2011b 3D tomographic image reconstruction from randomly ordered lines with CUDA GPU *Computing Gems Emerald Edition*, (New York: Elsevier) pp 679–91
- Pratx G, Surti S and Levin C 2011a Fast list-mode reconstruction for time-of-flight PET using graphics hardware *IEEE Trans. Nucl. Sci.* **58** 105–9
- Prenosil G A et al 2022 Performance characteristics of the biograph vision quadra PET/CT system with a long axial field of view using the NEMA NU 2-2018 standard *J. Nucl. Med.* **63** 476–84
- Rege S D et al 1993 Imaging of pulmonary mass lesions with whole-body positron emission tomography and fluorodeoxyglucose *Cancer* **72** 82–90
- Samanta S et al 2021 Performance comparison of a dedicated total breast PET system with a clinical whole-body PET system: a simulation study *Phys. Med. Biol.* **66** 115004
- Sarrut D et al 2014 A review of the use and potential of the GATE Monte Carlo simulation code for radiation therapy and dosimetry applications *Med. Phys.* **41** 064301
- Sarrut D et al 2021 Advanced Monte Carlo simulations of emission tomography imaging systems with GATE *Phys. Med. Biol.* **66** 10TR03
- Slomka P J, Pan T and Germano G 2016 Recent advances and future progress in PET instrumentation, in *Semin. Nucl. Med.* (WB Saunders) **46** 5–19
- Som P et al 1980 A fluorinated glucose analog, 2-fluoro-2-deoxy-D-glucose (F-18): nontoxic tracer for rapid tumor detection *J. Nucl. Med.* **21** 670–5
- Spencer B A et al 2021 Performance Evaluation of the uEXPLORER Total-Body PET/CT Scanner Based on NEMA NU 2-2018 with Additional Tests to Characterize PET Scanners with a Long Axial Field of View *J. Nucl. Med.* **62** 861–70
- Surti S 2015 Update on Time-of-Flight PET Imaging *J. Nucl. Med.* **56** 98–105
- Tai Y C, Wu H, Pal D and O'Sullivan J A 2008 Virtual-pinhole PET *J. Nucl. Med.* **49** 471–9
- Tan H et al 2020 Total-body PET/CT: current applications and future perspectives *American Journal of Roentgenology* **215** 325–37
- Vandenberghe S, Moskal P and Karp J S 2020 State of the art in total body PET *EJNMMI Phys.* **7** 1–33
- Viswanath V, Daube Witherspoon M E, Karp J S and Surti S 2020 Numerical observer study of lesion detectability for a long axial field-of-view whole-body PET imager using the PennPET Explorer *Phys. Med. Biol.* **65** 035002
- Weber W A 2010 Monitoring tumor response to therapy with 18F-FLT PET *J. Nucl. Med.* **51** 841–4
- Wu H, Pal D, Song T Y, O'Sullivan J A and Tai Y-C 2008 Micro Insert: a prototype full-ring PET Device for improving the image resolution of an animal PET scanner *J. Nucl. Med.* **49** 1668–76
- Zein S A, Karakatsanis N A, Issa M, Haj-Ali A A and Nehmeh S A 2020 Physical performance of a long axial field-of-view PET scanner prototype with sparse rings configuration: A Monte Carlo simulation study *Med. Phys.* **47** 1949–57
- Zhang J and Knopp M V 2020 *Advances in PET: The Latest in Instrumentation, Technology, and Clinical Practice* (Berlin:Springer Nature)
- Zhou J and Qi J 2009 Theoretical analysis and simulation study of a high-resolution zoom-in PET system *Phys. Med. Biol.* **54** 5193–208
- Zhu D et al 2017 Prognostic value of 18F-FDG-PET/CT parameters in patients with pancreatic carcinoma: A systematic review and meta-analysis *Medicine (Baltimore)* **96** e7813